



Photocatalytic degradation of 2,4-dichlorophenol on ZrO_2 - TiO_2 : influence of crystal size, surface area, and energetic states

Diana Guerrero-Araque¹ · David Ramírez-Ortega² · Próspero Acevedo-Peña³ · Rodolfo Zanella² · Ricardo Gómez⁴

Received: 14 November 2019 / Accepted: 6 January 2020 / Published online: 20 January 2020
© Springer Science+Business Media, LLC, part of Springer Nature 2020

Abstract

ZrO_2 - TiO_2 heterostructure with 5 mol% of ZrO_2 was synthesized by the sol-gel method and calcined at different temperatures (300–600 °C). The photocatalysts were characterized by thermal analysis, X-ray diffraction, physisorption of N_2 , diffuse reflectance spectroscopy, scanning electron microscopy, and X-ray photoelectron spectroscopy. The photocatalytic activity was tested for the removal of 2,4-dichlorophenol under ultraviolet irradiation, being the materials exhibiting the best performance those calcined at 400 °C and 500 °C with 99% and 98% of degradation, respectively, after 150 min under irradiation. This behavior was related to a smaller crystallite size, higher surface area, and significant hydroxyl radicals produced. The (photo)electrochemical study showed that temperatures of 400 °C and 500 °C also generated an optimum amount of energetic states that act as electron traps and decrease the electron-hole pair recombination, favoring the oxidation of 2,4-dichlorophenol. However, at 300 °C and 600 °C, these energetic states act as an energy barrier that reduces the effective charge transfer and therefore decreases the photocatalytic activity of the materials.

1 Introduction

TiO_2 is a semiconductor widely used in photocatalysis due to its chemical stability, abundance, low cost, and versatility in oxidation and reduction reactions. However, it presents a rapid recombination of photogenerated charge carriers, which decreases its photoactivity [1–3]. Several studies have reported the enhancement of photocatalytic activity when

TiO_2 is coupled with other metal oxides to form heterostructures [4, 5]. The efficiency of heterostructures depends on the oxide ratio, the band gap energy, and the relative conduction and valence bands positions [6–8]. It has been commonly reported that the photocatalytic performance in M_yO_x - TiO_2 heterostructures (M_yO_x : metal oxide semiconductor) is improved when the M_yO_x content is between 5–7 wt% [9–13].

In many cases, the photocatalytic activity has been attributed to parameters such as surface area, band gap energy, morphology, and/or crystallite size. However, although these parameters have high relevance, there is not always a clear relationship between them [14–16]. For example, Huang et al. related the improvement in the photocatalytic activity of Cu_2O/TiO_2 to band gap energies [17]; Shang et al. associated the increase in photocatalytic activity of Bi_2WO_6/TiO_2 with the surface area, grain size, and hierarchical heterostructure [18], while Strauss et al. showed that the smallest crystallite size of TiO_2 enhanced the oxidation of organic molecules due to a decrease in the recombination of photogenerated charge carriers [19].

Thus, to explain the photocatalytic performance of the semiconductors, some studies have focused on determining the semiconducting properties and flat band potential (E_{fb} , considered equivalent to Fermi level), as they determine

Electronic supplementary material The online version of this article (<https://doi.org/10.1007/s10854-020-02881-2>) contains supplementary material, which is available to authorized users.

✉ Diana Guerrero-Araque
dianacga@msn.com

- ¹ CONACyT- Universidad Autónoma Metropolitana, Departamento de Química, Av. San Rafael Atlixco 156, 09340 Mexico City, Mexico
- ² Instituto de Ciencias Aplicadas y Tecnología, Universidad Nacional Autónoma de México, Circuito Exterior S/N, Ciudad Universitaria, Coyoacán, 04510 Mexico City, Mexico
- ³ CONACyT-Instituto Politécnico Nacional, CICATA Unidad Legaria, 11500 Mexico City, Mexico
- ⁴ Universidad Autónoma Metropolitana, Departamento de Química, Av. San Rafael Atlixco 156, 09340 Mexico City, Mexico

driving forces of the electron transfer process [20]. In a previous study, ZrO₂–TiO₂ heterostructures, calcined at 500 °C with different contents of ZrO₂, were characterized using (photo) electrochemical techniques and evaluated for removal of pollutants in photocatalytic assays. The results showed changes in semiconducting properties of ZrO₂–TiO₂ heterostructures dependent on the ZrO₂ content, where the 5 wt% of ZrO₂ content proved to exhibit the best activity. This behavior was attributed to the formation of surface energy states between the grain boundaries of their components that act as electron traps favoring the charge carrier separation. However, during the photo-irradiation at higher ZrO₂ contents, these states act as recombination centers [21].

On the other hand, it has been reported that calcination temperature modifies the performance of photocatalysts in the oxidation of pollutants. Siwinska-Stefanska et al. [22] found that TiO₂–ZnO calcined at 600 °C had the best performance in the degradation of three organic dyes compared with pristine TiO₂, despite the decrease in its specific surface area. The present work reports the effect of calcination temperature on ZrO₂–TiO₂ photocatalyst with 5 wt% of ZrO₂ in photodegradation of 2,4-dichlorophenol. (Photo) electrochemical studies were carried out to understand the effect of heat treatment on the semiconductor properties of the photocatalysts.

2 Experimental

2.1 Synthesis of ZrO₂–TiO₂

ZrO₂–TiO₂ photocatalyst (ZT) was prepared by the sol–gel method, as reported elsewhere [21]. For the synthesis, titanium *n*-butoxide, zirconium *n*-butoxide (5 mol% of ZrO₂), *n*-butanol, and nitric acid were mixed. Then, 8 mol of deionized water were added to the reaction system. The mixture was refluxed at 80 °C for 24 h. The resulting solid was washed with water, dried and calcined in air at 300 °C, 400 °C, 500 °C, and 600 °C for 4 h.

2.2 Characterization

Thermogravimetric analysis was performed on a Shimadzu DT-30 analyzer. The material was heated until 800 °C in air atmosphere with a temperature ramp of 10 °C/min. All photocatalysts were characterized using a Bruker D2 Phaser diffractometer with a source of CuK α radiation ($\lambda = 0.154$ nm); the crystallite sizes were calculated by Scherrer equation. The band gap values were estimated using a Varian Cary 100 spectrophotometer, equipped with an integrating sphere using BaSO₄ as reference. The textural properties were obtained by a Micromeritics ASAP-2000 analyzer. A Jeol7600F microscope was employed for SEM analysis. XPS

was carried out using a K-alpha Thermo Fisher Scientific spectrometer.

2.3 Photocatalytic activity

The degradation of 2,4-dichlorophenol (2,4-DCP) was evaluated in solutions of 200 mL, with an initial concentration of 40 ppm. The solutions were stirred in a home-made reactor for 30 min in the dark to allow adsorption–desorption equilibrium of the pollutant on the solid. Afterward, solutions were irradiated with UV light for 150 min using a Pen-Ray lamp of $I = 7.6$ mW/cm². The progress of the reaction was monitored with a Cary 100 spectrophotometer by following the main absorption band as a function of the irradiation time, at 284 nm. The total organic carbon (TOC) concentration of the samples was measured using a TOC–V_{CSN} analyzer Shimadzu. Additionally, the production of hydroxyl radicals was determined through the fluorescence spectra of 2-hydroxyterephthalic acid in a SCINCO fluorescence spectrometer FS-2 as follows: terephthalic acid (TA) (5×10^{-4} M) was dissolved in a water/NaOH solution (2×10^{-3} M), then 100 mg of photocatalyst were added, and the suspension was stirred for 30 min under dark condition. Afterward, it was irradiated by a UV light Pen-Ray lamp, during 30 min, and aliquots were taken every 5 min.

2.4 Electrochemical characterization

Electrochemical measurements were carried out in a conventional three-electrode cell using the films of calcined materials as working electrodes, graphite rod as a counter electrode, and an Ag/AgCl 3 M KCl as a reference electrode. The working electrodes were prepared as follows: 10 mg of the photocatalyst were dispersed into a solution of the ethanol–nafion mixture, after the mixture was maintained under sonication at room temperature during 30 min. Then, 5 μ L of the mixture was coated onto ITO. The resulting electrodes were dried at room temperature during 24 h.

3 Results and discussion

To identify the transformation of ZT photocatalyst with the heating, simultaneous TGA/DTG were measured under air flow (5 °C/min) (Fig. 1). The weight loss measured by TGA corresponds to several peaks observed in the DTG. The first peak between 20–90 °C, with a weight loss of 4.5%, is associated with the removal of physisorbed water on the surface of the photocatalyst. In the range of 90–310 °C, the peaks with maxima at 200 °C and 278 °C, and a combined weight

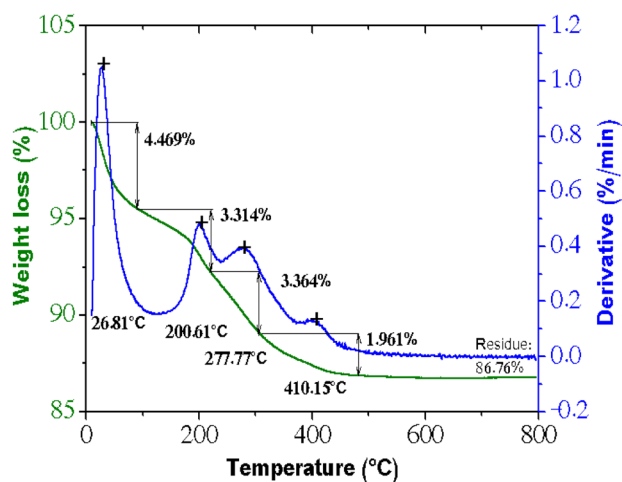


Fig. 1 Thermogravimetric analysis TGA and derivative weight loss curves of ZT photocatalyst

loss of 6.7% can be attributed to the combined loss of water and residual organics from the synthesis.

Moreover, a small peak was observed between 380 and 450 °C, with a maximum at 410 °C, related to the crystallization of the material. The total weight loss for the material heated up to 800 °C, as determined by TGA, was 13% and it mainly takes place below 400 °C. The remaining 1% weight loss above 400 °C is due to the elimination of chemisorbed hydroxyl groups that react to form additional M–O–M bonds through condensation and elimination of H₂O. These results are relevant since a specific crystalline phase, and a significant density of hydroxyl groups have been recognized to improve photocatalytic activity [23].

Thus, to establish the resulting crystalline phases in ZT calcined at different temperatures, XRD measurements were performed, Fig. S1. Calcined materials show the characteristic diffraction peaks at $2\theta = 25.3^\circ, 37.8^\circ, 47.9^\circ, 53.9^\circ, 62.6^\circ, 68.8^\circ,$ and 75.6° , corresponding to anatase phase of TiO₂ [24], while peaks corresponding to ZrO₂ were not observed. These results coincide with a previous study, where diffraction peaks were not seen in the material with 5wt% of ZrO₂ content; nonetheless, the formation of ZrO₂–TiO₂ heterojunctions was proved through TEM [21]. As has already

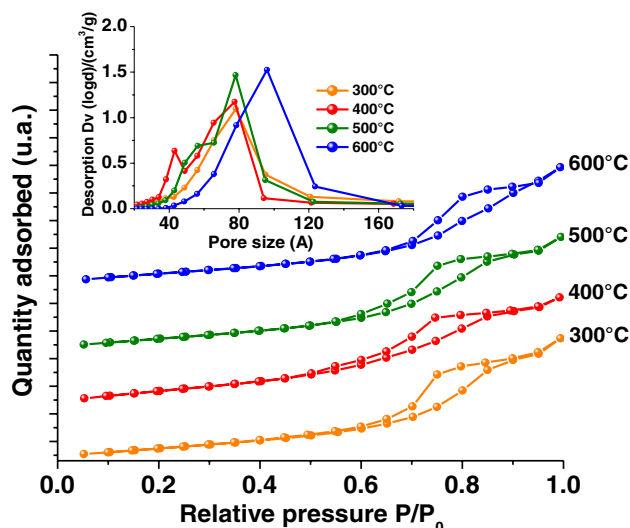


Fig. 2 N₂ adsorption–desorption isotherms and pore size distribution plots of ZT photocatalysts calcined at different temperatures

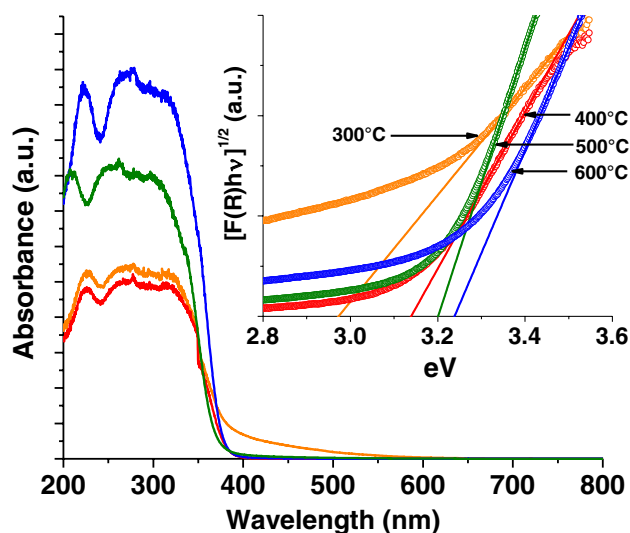


Fig. 3 UV–Vis spectra and Tauc plot of the ZT photocatalysts calcined at different temperatures

Table 1 Structural, textural, and optical properties of the synthesized materials

Materials	$D_{(101)}$ [*] (nm)	S_{BET} [‡] (m ² /g)	d_{pore} [‡] (nm)	V_{pore} [‡] (cm ³ /g)	E_g [†] (eV)
ZT-300 °C	11.73	170	7.7	0.3329	2.97
ZT-400 °C	8.86	173	7.7	0.3340	3.14
ZT-500 °C	8.92	150	7.8	0.3482	3.17
ZT-600 °C	9.66	152	7.8	0.3465	3.24

^{*}Estimated from FWHM peak in XRD patterns using the Scherrer equation

[‡]Estimated by BET N₂ adsorption method

[†]Estimated by diffuse reflectance spectra

been recognized, the TiO_2 undergoes a phase transformation from anatase to rutile, beginning at 500 °C [25, 26]. However, despite the increase in calcination temperature until 600 °C, the rutile phase was not observed since the inclusion of ZrO_2 is known to prevent the formation of rutile [27]. Additionally, the crystallite size slightly decreased until 500 °C and subsequently, slightly increased at 600 °C, which may be attributed to a thermally promoted growth (Table 1) [28].

The specific surface area is considered as an important factor for photocatalytic materials; thus, N_2 adsorption measurements were carried out. Typical type IV isotherms were observed in all photocatalysts with H_2 type hysteresis loop which is a characteristic of mesoporous materials (Fig. 2). Higher specific surface area values than pristine materials ($\text{TiO}_2 = 50 \text{ m}^2/\text{g}$ and $\text{ZrO}_2 = 45 \text{ m}^2/\text{g}$) (Table 1)

were obtained for all the composites; however, the specific surface area decreased with the increase in calcination temperature, which is explained by the collapse of some pores in the materials. Regarding to the pore size distributions of the as-synthesized materials, all possess very narrow distributions entirely located in the mesoporous region, as is most clearly seen in the inset in Fig. 2 [29, 30].

The impact of the final temperature in the calcination process on the optical properties of the materials was analyzed by determining the band gap energy through diffuse reflectance measurements (Fig. 3). The band gap values (estimated by UV–Vis) are close to the one of TiO_2 because it is the main component in the $\text{ZrO}_2\text{–TiO}_2$ photocatalysts. Besides, other factors that may be related to the slight rise in optical band gap with increased heating include a variation in the particle size, crystal density due to the variation

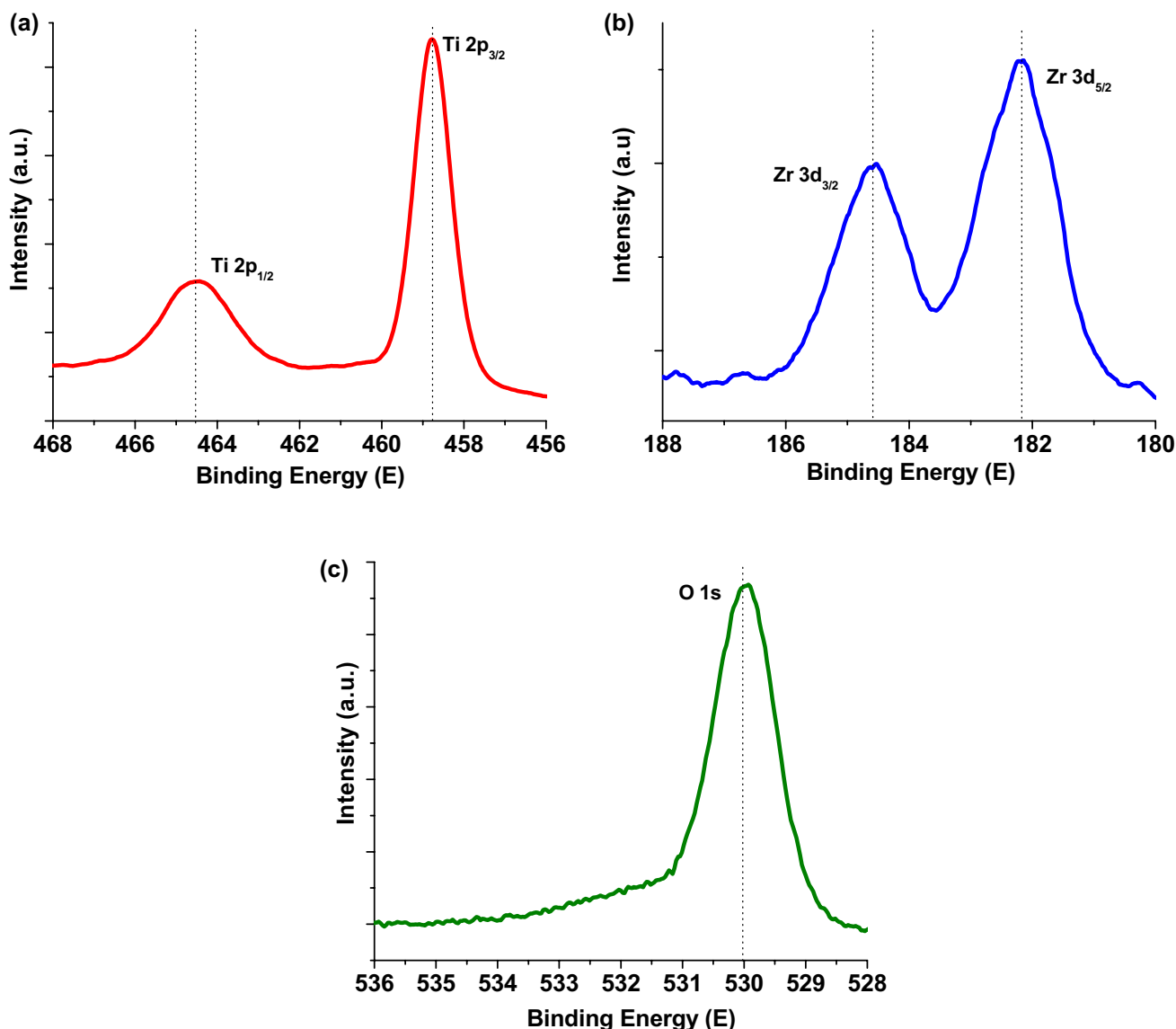


Fig. 4 XPS analysis: a Ti 2p, b Zr 3d, and c O 1s spectra of ZT photocatalyst calcined at 400 °C

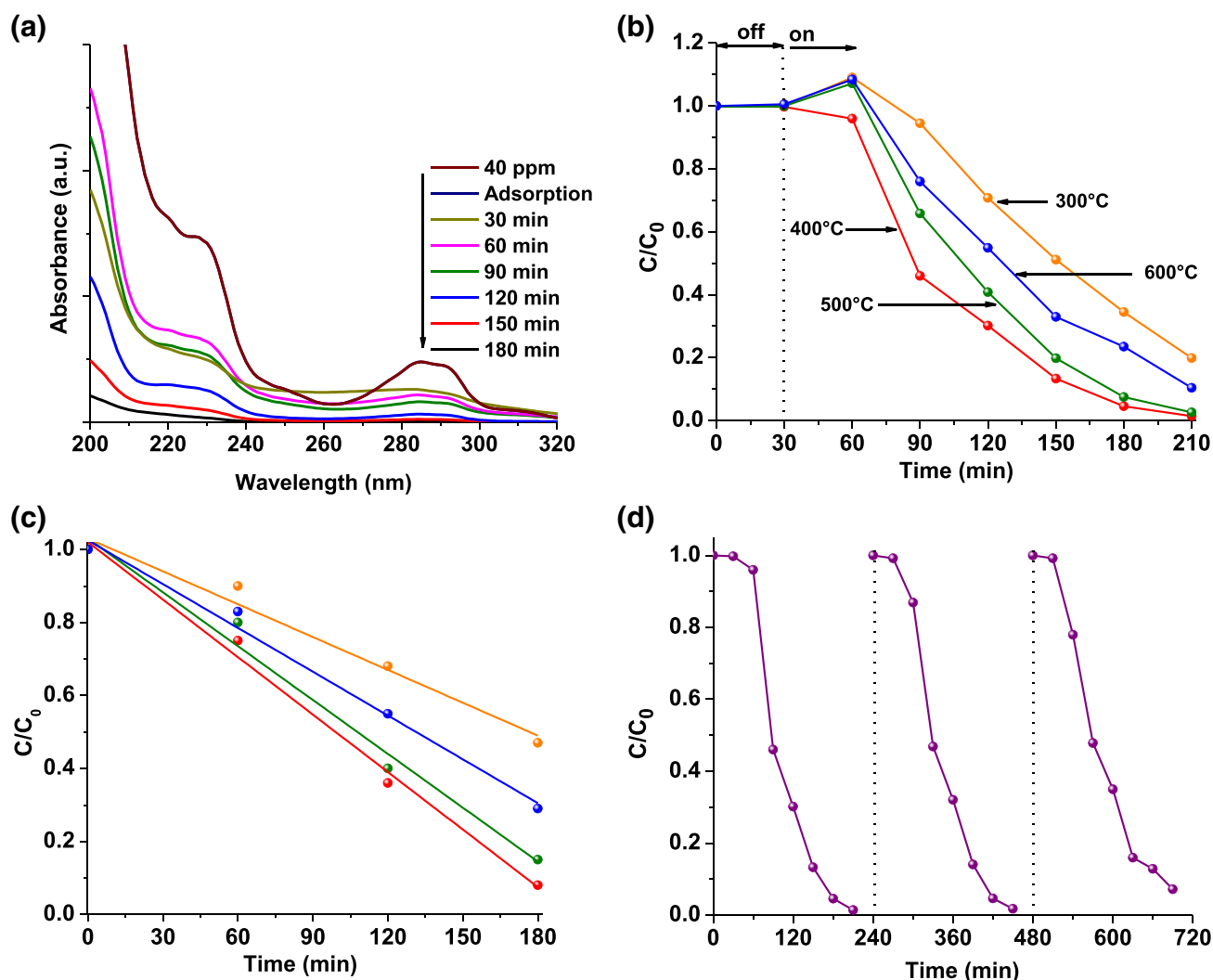


Fig. 5 **a** UV–Vis absorbance spectra obtained during photocatalytic degradation of 2,4-DCP with ZT calcined at 400 °C under UV irradiation measured at different times; **b** Relative concentration of 2,4-

DCP employing ZT photocatalysts calcined at different temperatures; **c** Pseudo-zero order kinetics; and **d** Reusability of ZT photocatalyst calcined two times at 400 °C

Table 2 Rate constants of pseudo-zero order R^2 in the degradation of 2,4-DCP

Materials	k (min^{-1})	R^2
ZT-300 °C	-0.003	0.972
ZT-400 °C	-0.00525	0.989
ZT-500 °C	-0.00492	0.977
ZT-600 °C	-0.004	0.989

of oxygen vacancies, and defects in the materials originated by calcination process [21, 31]. Kumar et al. mentioned that the quantity of oxygen vacancies is related to the calcination process, changing the electronic levels between the valence and conduction band of the semiconductor; these vacancies can also modify the recombination process [32].

On the other hand, Fig. S2 shows the SEM images of the ZT photocatalyst calcined at 400 °C. The photocatalyst

consists of agglomerates of irregular shape created during the washing process and the thermal treatment. This aggregation leads to the formation of a mesoporous structure in the as-synthesized materials as confirmed by BET measurements. Also, the elemental composition showed a homogeneous distribution of Ti, O, and Zr in the material [33].

The surface chemical composition of the ZT photocatalyst calcined at 400 °C was established using X-ray photoelectron spectroscopy (Fig. 4). The signals of Ti $2p_{1/2}$ and Ti $2p_{3/2}$ are 458.76 eV and 464.66 eV, respectively; the peak separation of 5.9 eV between the signals of Ti $2p_{1/2}$ and Ti $2p_{3/2}$ allows inferring that the oxidation state of titanium is Ti^{4+} (Fig. 4a) [34, 35]. However, the Zr 3d signals for ZT photocatalyst show two peaks at 182.18 eV and 184.53 eV, corresponding to $3d_{5/2}$ and $3d_{3/2}$ of Zr^{4+} , respectively (Fig. 4b) [36, 37]. This result confirms the presence of zirconium oxide in the

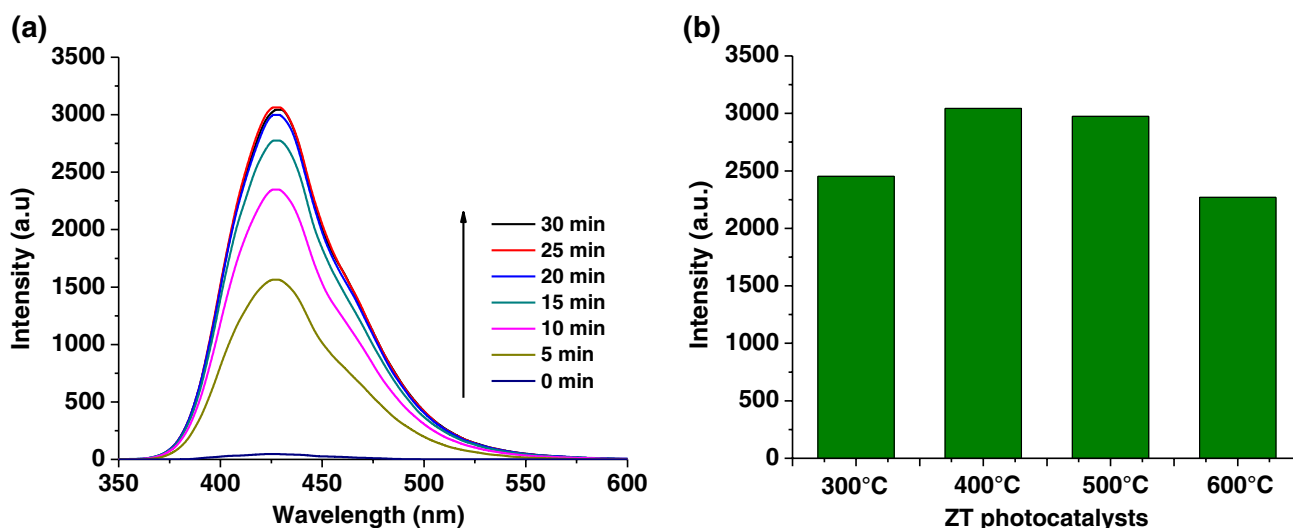


Fig. 6 a Fluorescence spectra of terephthalic acid with the ZT photocatalyst calcined at 400 °C and b Comparative hydroxyl radicals formed for ZT photocatalysts

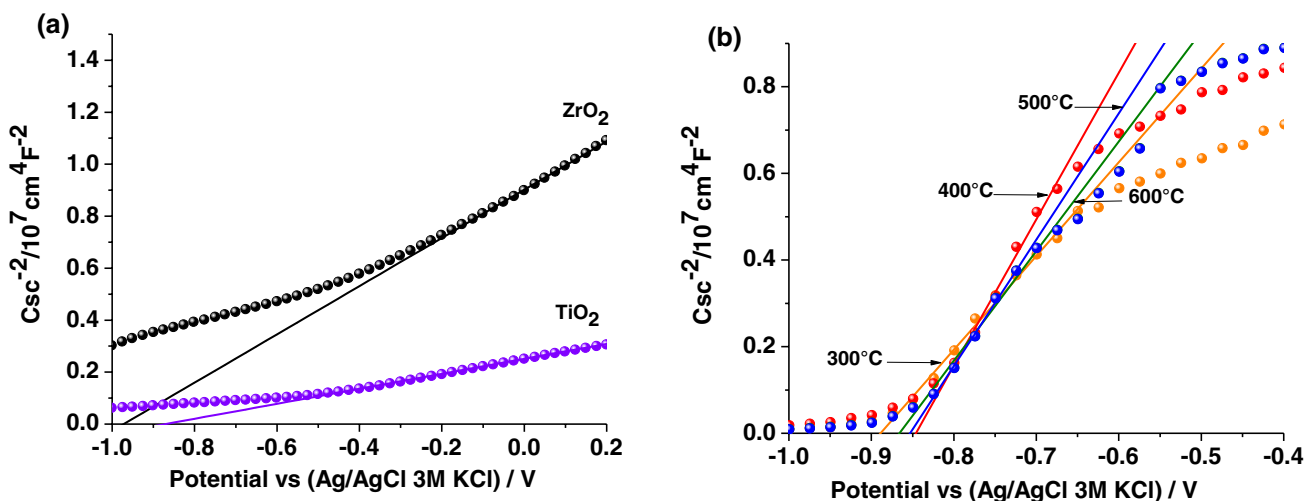


Fig. 7 Mott-Schottky plots of ZrO₂-TiO₂ photocatalyst calcined at different temperatures: a 300 °C, b 400 °C, c 500 °C, and d 600 °C. The Csc were obtained at 100 Hz in 0.03 M KClO₄ (pH 6.0) aqueous solution

photocatalyst even though it was not observed by XRD (Fig. S1). The O 1s presents two contributions at 529.95 eV and 532.0 eV, assigned to bulk oxide (O²⁻) and hydroxyl (OH⁻) species, respectively (Fig. 4c) [34]. Also, the distinct signal of hydroxyl groups observed is associated with the surface defects of the material [38].

3.1 Photocatalytic activity

The photocatalytic performance of ZT photocatalysts was evaluated by 2,4-dichlorophenol (2,4-DCP) degradation under UV irradiation. In brief, 100 mg of the photocatalyst were added to 2,4-DCP solution (40 ppm), and the mixture

was stirred for 30 min in the dark to allow the adsorption-desorption equilibrium of organic compound on the solid. Figure 5a shows the evolution of degradation using the material calcined at 400 °C during 150 min of illumination, and Fig. 5b displays the results of the activity of the evaluated photocatalysts. The assays exhibit an improvement in the photocatalytic activity when the temperature of calcination increases from 300 to 400 °C, but beyond this point, the photocatalytic degradation of 2,4-DCP declines. The activity of materials can be related to the crystallite size, surface area, and the content of surface defects that affect the separation of photogenerated carriers. It is known that an increase in the temperature of calcination provokes a

Scheme 1 Energy scheme of pristine TiO_2 , ZrO_2 , and ZT photocatalysts and their interaction for spatial separation of photogenerated charge carriers

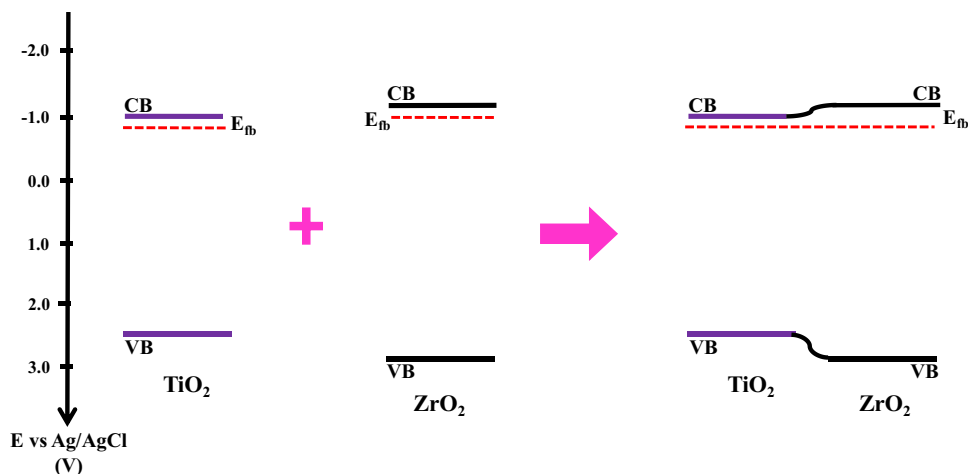


Table 3 Flat band potential (E_{fb}) and donor density (N_d) of ZT photocatalysts

Materials	E_{fb} (v)	N_d ($\times 10^{18} \text{ cm}^{-3}$)
ZT-300 °C	-0.88	7.86
ZT-400 °C	-0.84	5.03
ZT-500 °C	-0.85	5.83
ZT-600 °C	-0.86	6.29

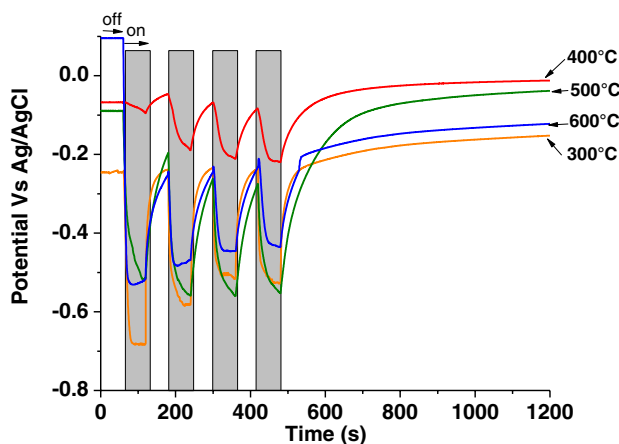


Fig. 8 OCP measurements in the dark (off) and under UV illumination (on) for ZrO_2 - TiO_2 photocatalysts calcined at 300 °C, 400 °C, 500 °C, and 600 °C

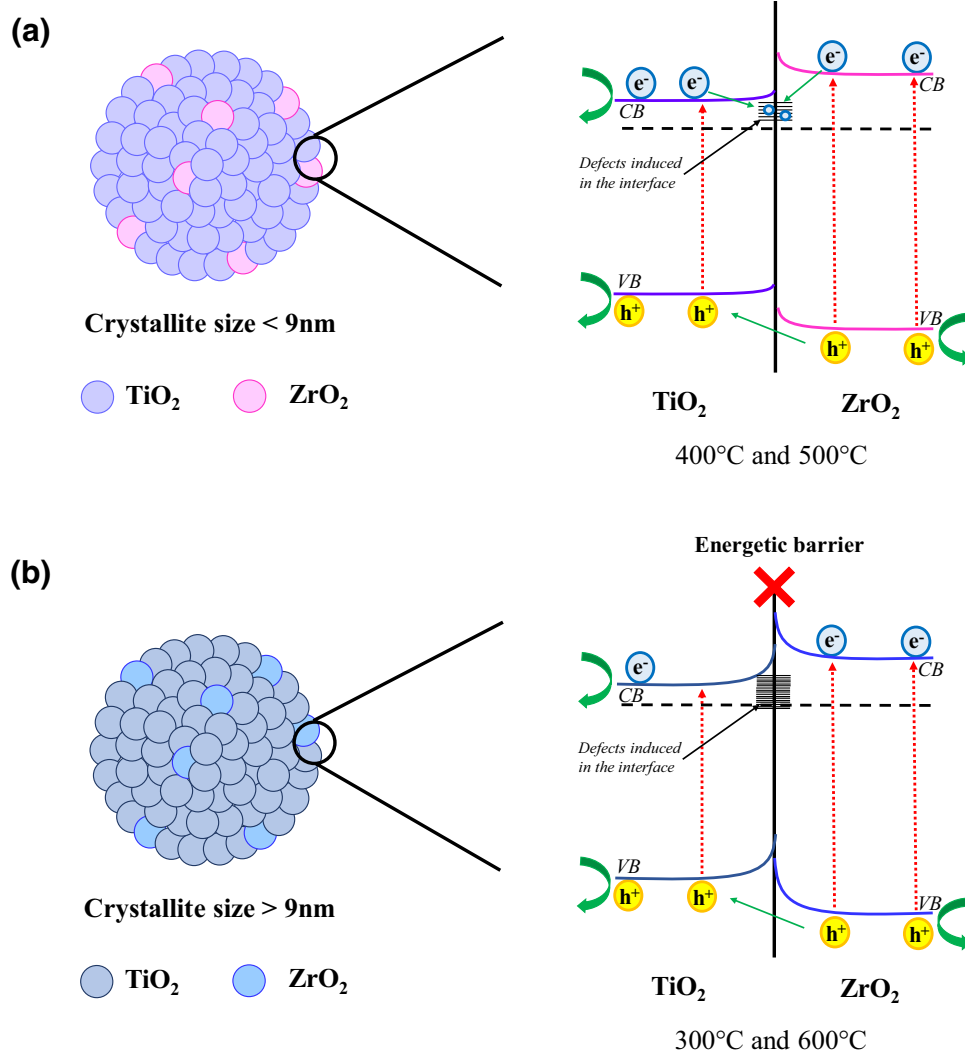
decrease in oxygen vacancies [39, 40]. However, it is important to mention that the 2,4-DCP degradation by photolysis was negligible and that all ZT photocatalysts showed a higher photoactivity than photolysis. On the other hand, total organic carbon (TOC) concentration of the samples taken in the assays showed the same tendency as UV-Vis measurements (Fig. 5c). However, it is not possible to establish

the kinetics behavior of 2,4-DCP degradation by UV-Vis spectroscopy as a function of time, due to the formation of intermediate products and to the complexity of the spectra. Thus, the degradation of 2,4-DCP was monitored by means of TOC measurements which determine the degree of mineralization of the molecule. The mineralization of 2,4-DCP has a pseudo-zero order kinetic indicating that the reaction rate is independent of the concentration of molecule in the solution. The kinetic parameters are summarized in Table 2. The stability of ZT photocatalyst calcined at 400 °C was studied by repeating the test two times. The results showed that the photocatalytic degradation remained almost unchanged implying that this material is stable and reusable (Fig. 5d).

Hydroxyl radicals are considered as some of the most powerful oxidizing agents that react with organic pollutants. Thus, to establish the formation of hydroxyl radicals during the illumination, terephthalic acid fluorescence tests were carried out [41]. In the assays, the hydroxyl radicals react with the terephthalic acid giving rise to 2-hydroxyterephthalic acid, which emits a single fluorescence signal at 426 nm. Figure 6a shows the growth of fluorescence intensity as a function of irradiation time employing the material calcined at 400 °C. The increase in signal is associated with a rise in the amount of hydroxyl radicals formed. At the same time, Fig. 6b shows the final intensity of all ZT photocatalysts, being the material calcined at 400 °C the one with the highest production of hydroxyl radicals. These results coincide with the tendency obtained in the degradation tests implying that the higher the number of hydroxyl radicals, the greater the degradation of 2,4-DCP [42].

To establish the relationship between the semiconducting properties of the materials and their photocatalytic activity, films of pristine TiO_2 , ZrO_2 , and ZT photocatalysts were characterized by EIS measurements and flat band potentials (E_{fb}) were obtained from Mott-Schottky plots (Fig. 7). Flat band potential value is considered as an approximation of conduction band position, being in this case -0.84 V for

Scheme 2 Energy diagram illustrating the coupling of ZrO_2 – TiO_2 photocatalysts calcined at different temperatures



TiO_2 and -0.97 V for ZrO_2 (Fig. 7a). Subtracting the band gap energies from the E_{fb} values, the valence band can be localized. In this sense, in ZT photocatalysts, the photogenerated electrons and holes will be transported from ZrO_2 to TiO_2 [43]. The alignment of Fermi levels of TiO_2 and ZrO_2 in the photocatalysts provokes a change in E_{fb} values compared with pristine materials, whereas the E_{fb} values of ZT photocatalysts vary from one to another with calcination temperature (Scheme 1). In the sample heat-treated at 400 °C, a slight change towards a less negative value of flat band potential was observed, while at higher temperatures a change towards more negative values occurred (Fig. 7b) [44]. The shift in flat band potentials can be associated with a change of surface defects in the material, originated by the calcination process. However, to establish the cause of the best performance at 400 °C, number donors (N_d) were analyzed because of the relationship between energetic states and modification of free carrier density [45]. As is observed in Table 3, the photocatalyst calcined at 400 °C has

the lowest N_d implying that in spite of the same composition of the photocatalyst, the calcination temperature provokes a decrease in the defect sites, and the optimum donor density is the factor that impacts the photocatalytic activity. In a previous study, the lowest N_d was observed to give rise to the highest activity [12, 46].

Furthermore, to elucidate the behavior of photogenerated electrons under irradiation and dark conditions, open circuit potential (OCP) experiments were carried out in oxygen-free solutions. Figure 8 shows that, under illumination, the OCP drops immediately towards more negative values; it is related to the accumulation of electrons in the conduction band reaching a balancing rate between creation and deletion of photogenerated electrons [47]. Moreover, as calcination temperature increases, the electrons occupy lower energy levels recognized as defects (or traps), which are originated by the heating process. However, it is important to note that in the photocatalyst calcined at 400 °C, the OCP values become less negative.

The previously discussed results suggest that thermal conditions fix the final characteristics of photocatalysts. Under the irradiation of UV light, photogenerated holes react with water molecules to produce $\cdot\text{OH}$ radicals and simultaneously, the electrons captured in the surface states can react with dissolved oxygen molecules to generate $\text{O}_2^{\cdot-}$ radical ions that could result in more $\cdot\text{OH}$ radicals. In this case, the catalyst features as band gap, surface area, crystallite size, interfacial defects, and band alignment can be tuned by modifications upon heat treatment. The materials calcined at 400 °C and 500 °C were found to exhibit the highest activity due to their high specific surface area, small crystallite size, and a significant hydroxyl radical production [48, 49]. The (photo)electrochemical measurements showed the presence of energetic states in the $\text{ZrO}_2\text{-TiO}_2$ interface. These energy states can be created on the surface or at the grain boundaries of contact between TiO_2 and ZrO_2 acting as electron traps that promote the separation of electron–hole pairs under irradiation, which remarkably improves the photocatalytic activity [50]. As illustrated in Scheme 2, calcination temperatures of 400 °C and 500 °C favor the oxidation process due to optimum quantity of surface states, lower crystallite sizes, high surface area, and significant hydroxyl radical production, thus creating a higher number of active sites. However, in the photocatalysts calcined at 300 °C and 600 °C, the energetic states generate an energy barrier that decreases the photocatalytic activity.

4 Conclusion

The synthesis of $\text{ZrO}_2\text{-TiO}_2$ heterostructures is a good strategy for enhancing the activity of pristine TiO_2 . The inclusion of ZrO_2 decreases the crystallite size of TiO_2 and delays the appearance of rutile phase despite the heating process. At the same time, the increase in surface area favors the creation of a higher number of active sites. The amount of energy states depends on the calcination temperature. These states act as electron traps minimizing the charge recombination, resulting in increased photocatalytic removal of 2,4-dichlorophenol. At temperatures above 500 °C, the surface states act as an energy barrier that limits the photoactivity of ZT photocatalyst.

Acknowledgements The authors thank the Laboratorio Universitario de Caracterización Espectroscópica (LUCE-UNAM) and Laboratorio Universitario de Nanotecnología Ambiental (LUNA-UNAM) as well as V. Maturano and S. Islas for technical support. We also thank CONACyT for financial support granted through the project CB-2015-01 256410 Synthesis of hybrid Materials. Materials for Alternative energies. SEP-Profides 2018, UANL-UAM.CB-2015-01 256410. D.A. Ramírez Ortega (CVU 329398) thanks CONACyT for post-doctoral grant.

Compliance with ethical standards

Conflict of interest The authors declare that the contents of this work have no conflict of interest with any individual or organization.

References

1. B. Zhang, S. Cao, M. Du, X. Ye, Y. Wang, J. Ye, *Catalysts* **9**, 1–27 (2019)
2. X. Ba, L. Yang, A. Hagfeldt, E.M.J. Johansson, P. Jin, *Chem. Eng. J.* **355**, 999–1010 (2019)
3. J. Zhao, P. Zhang, Z. Wang, S. Zhang, H. Gao, J. Hu, G. Shao, *Sci. Rep.* **7**, 1–11 (2017)
4. W. Zhou, H. Liu, J. Wang, D. Liu, G. Du, J. Cui, *ACS Appl. Mater. Interfaces* **2**, 2385–2392 (2010)
5. L. Shi, C. Xu, X. Sun, H. Zhang, Z. Liu, X. Qu, F. Du, *J. Mater. Sci.* **53**, 11329–11342 (2018)
6. H. Cai, L. Cheng, F. Xu, H. Wang, W. Xu, F. Li, *R. Soc. Open Sci.* **5**, 1–11 (2018)
7. N. Talinungsang, D.D. Paul, M.G. Purkayastha, *Superlattices Microstruct.* **129**, 105–114 (2019)
8. L. Baia, E. Orbán, S. Fodor, B. Hampel, E.Z. Kedves, K. Saszet, I. Székely, É. Karácsonyi, B. Réti, P. Berki, A. Vulpoi, K. Magyarai, A. Csavdári, C. Bolla, V. Coşoveanu, K. Hernádi, M. Baia, A. Dombi, V. Danciu, G. Kovács, Z. Pap, *Mater. Sci. Semicond. Proc.* **42**, 66–71 (2016)
9. M.A. Ahmed, E.E. El-Katori, Z.H. Gharni, *J. Alloys Compd.* **553**, 19–29 (2013)
10. C. Moslah, T. Aguilar, R. Alcántara, M. Ksibi, J. Navas, *J. Chin. Chem. Soc.* **66**, 99–109 (2019)
11. K.Y. Jung, S.B. Park, S.K. Ihm, *Appl. Catal. B* **51**, 239–245 (2004)
12. D. Ramírez-Ortega, A.M. Meléndez, P. Acevedo-Peña, I. González, R. Arroyo, *Electrochim. Acta* **140**, 541–549 (2014)
13. D. Ramírez-Ortega, P. Acevedo-Peña, F. Tzompantzi, R. Arroyo, I. González, *J. Mater. Sci.* **52**, 260–275 (2017)
14. B. Mazinani, A.K. Masrom, A. Beitollahi, R. Luque, *Ceram. Int.* **40**, 11525–11532 (2014)
15. M. Rosales, T. Zoltan, C. Yadarola, E. Mosquera, F. Gracia, A. García, *J. Mol. Liq.* **281**, 59–69 (2019)
16. S. Wang, P. Kuang, B. Cheng, J. Yu, C. Jiang, *J. Alloys Compd.* **741**, 622–632 (2018)
17. L. Huang, F. Peng, H. Wang, H. Yu, Z. Li, *Catal. Commun.* **10**, 1839–1843 (2009)
18. M. Shang, W. Wang, L. Zhang, S. Sun, L. Wang, L. Zhou, *J. Phys. Chem. C* **113**, 14727–14731 (2009)
19. M. Strauss, M. Pastorello, F.A. Sigoli, J.M. de Souza e Silva, I.O. Mazali, *Appl. Surf. Sci.* **319**, 151–157 (2014)
20. P. Xu, T.J. Milstein, T.E. Mallouk, A.C.S. Appl. Mater. Interfaces **8**, 11539–11547 (2016)
21. D. Guerrero-Araque, D. Ramírez-Ortega, P. Acevedo-Peña, F. Tzompantzi, H.A. Calderón, R. Gómez, *J. Photochem. Photobiol. A* **335**, 276–286 (2017)
22. K. Siwinska-Stefanska, A. Kubiak, A. Piasecki, J. Goscianska, G. Nowaczyk, S. Jurga, T. Jesionowski, *Materials* **11**, 1–19 (2018)
23. C.Y. Wu, K.J. Tu, J.P. Deng, Y.S. Lo, C.H. Wu, *Materials* **10**, 566 (2017)
24. X. Liang, P. Wang, M. Li, Q. Zhang, Z. Wang, Y. Dai, X. Zhang, Y. Liu, M.H. Whangbo, B. Huang, *Appl. Catal. B* **220**, 356–361 (2018)
25. M. Dahl, Y. Liu, Y. Yin, *Chem. Rev.* **114**, 9853–9889 (2014)
26. X. Chen, X. Wang, X. Fu, *Energy Environ. Sci.* **2**, 872–877 (2009)

27. D.A.H. Hanaor, C.C. Sorrell, *J. Mater. Sci.* **46**, 855–874 (2011)
28. Y.F. Chen, C.Y. Lee, M.Y. Yeng, C.H. Chiu, *J. Cryst. Growth* **247**, 363–370 (2003)
29. J.G. Yu, H.G. Yu, B. Cheng, X.J. Zhao, J.C. Yu, W.K. Ho, *J. Phys. Chem. B* **107**, 13871–13879 (2003)
30. X. You, F. Chen, J. Zhang, *J. Sol Gel Sci. Technol.* **34**, 181–187 (2005)
31. Z.N. Kayani, F. Saleemi, I. Batool, *Appl. Phys. A* **119**, 713–720 (2015)
32. S. Kumar, S. Bhunia, A.K. Ojha, *Physica E* **66**, 74–80 (2015)
33. L. Kokporka, S. Onsuratoom, T. Puangpetch, S. Chavadej, *Mater. Sci. Semicond. Proc.* **16**, 667–678 (2013)
34. B. Erdem, R.A. Hunsicker, G.W. Simmons, E.D. Sudol, V.L. Dimonie, M.S. El-Aasse, *Langmuir* **17**, 2664–2669 (2001)
35. B.M. Reddy, A. Khan, Y. Yamada, T. Kobayashi, S. Loridant, J.V. Volta, *J. Phys. Chem. B* **107**, 5162–5167 (2003)
36. A. Sinhamahapatra, J.P. Jeon, J. Kang, B. Han, J.S. Yu, *Sci. Rep.* **6**, 27218 (2016)
37. A. Juma, I.O. Acik, A.T. Oluwabi, A. Mere, V. Mikli, M. Danilson, M. Krunk, *Appl. Surf. Sci.* **387**, 539–545 (2016)
38. J. Yan, G. Wu, N. Guan, L. Li, Z. Li, X. Cao, *Phys. Chem. Chem. Phys.* **15**, 10978–10988 (2013)
39. L. He, Z. Tong, Z. Wang, M. Chen, N. Huang, W. Zhang, *J. Colloid Interface Sci.* **509**, 448–456 (2018)
40. J. Xu, Y. Teng, F. Teng, *Sci. Rep.* **6**, 32457 (2016)
41. S. Gligorovski, R. Strekowski, S. Barbati, D. Vione, *Chem. Rev.* **115**, 13051–13092 (2015)
42. D. Zhang, R. Qiu, L. Song, B. Eric, Y. Mo, X. Huang, *J. Hazard. Mater.* **163**, 843–847 (2009)
43. A. Kambur, G.S. Pozan, I. Boz, *Appl. Catal. B* **115–116**, 149–158 (2012)
44. M. Ismael, M. Wark, *Catalysts* **9**, 342 (2019)
45. M.F.M. Noh, M.F. Soh, C.H. Teh, E.L. Lim, C.C. Yap, M.A. Ibrahim, N.A. Ludin, M.A.M. Teridi, *Sol. Energy* **158**, 474–482 (2017)
46. J.Q. Lu, T.E. Kopley, N. Moll, D. Roitman, D. Chamberlin, Q. Fu, J. Liu, T.P. Russell, D.A. Rider, I. Manners, M.A. Winnik, *Chem. Mater.* **17**, 2227–2231 (2005)
47. S. Li, Q. Wang, T. Chen, Z. Zhou, Y. Wang, J. Fu, *Nanoscale Res. Lett.* **7**, 227 (2007)
48. S.H. Othman, S.A. Rashid, T.I. Mohd Ghazi, N. Abdullah, *J. Nanomater.* **512785**, 1–10 (2010)
49. M. Hamadianian, A. Reisi-Vanani, A. Majedi, *Mater. Chem. Phys.* **116**, 376–382 (2009)
50. X. Yu, B. Kim, Y.K. Kim, *ACS Catal.* **3**, 2479–2486 (2013)

Publisher's Note Springer Nature remains neutral with regard to jurisdictional claims in published maps and institutional affiliations.